*Article*

# Photodegradation and Mineralization of Phenol Using TiO₂ Coated γ-Al₂O₃: Effect of Thermic Treatment

Claudia Martinez-Gómez [1,*] , Israel Rangel-Vazquez [2], Ramon Zarraga [1], Gloria del Ángel [2], Beatriz Ruíz-Camacho [3], Francisco Tzompantzi [2], Esmeralda Vidal-Robles [4] and Alejandro Perez-Larios [5,*]

[1] Department of Chemistry, Division of Natural and Exact Sciences, Campus Guanajuato, University of Guanajuato, Noria Alta S/N, Col. Noria Alta, Guanajuato 36050, Guanajuato, Mexico; rzarraga@ugto.mx

[2] Laboratory of Catalysis, Department of Chemistry, Division of Basic Sciences and Engineering, Universidad Autónoma Metropolitana-Iztapalapa, Av. San Rafael Atlixco No. 186, Mexico City 09340, Mexico; isradt@hotmail.com (I.R.-V.); gdam@xanum.uam.mx (G.d.Á.); fjtz@xanum.uam.mx (F.T.)

[3] Department of Chemical Engineering, Division of Natural and Exact Sciences, Campus Guanajuato, University of Guanajuato Noria Alta S/N, Col. Noria Alta, Guanajuato 36050, Guanajuato, Mexico; beatriz.ruiz@ugto.mx

[4] Faculty of Chemical Engineering, Benemérita Universidad Autónoma de Puebla, Ciudad Universitaria Av. Sn. Claudio y, Blvd. 18 Sur Col, Jardines de San Manuel, Puebla 72570, Puebla, Mexico; esmeralda.vidal@correo.buap.mx

[5] Nanomaterials, Water and Energy Research Laboratory, Department of Engineering, Centro Universitario de los Altos, Universidad de Guadalajara, Av. Rafael Casillas Aceves 1200, Tepatitlán de Morelos 47600, Jalisco, Mexico

\* Correspondence: claudia.martinez@ugto.mx (C.M.G.); alarios@cualtos.udg.mx (A.P.-L.)

**Abstract:** It is well-known that γ-Al₂O₃ possesses large, specific areas and high thermal, chemical, and mechanical resistance. Due to this, it is the most-used support for catalysts, in this case TiO₂, as it enables it to achieve better dispersion and improves the activity in catalytic photodegradation reactions. In a previous work, it was observed that the optimal content of TiO₂ in γ-Al₂O₃ was around 15% since the degradation of phenol results were maximized and a synergistic effect was generated by the interaction of both oxides. In addition, an increase in acidity crystal size and the generation of localized, oxygen-vacant, electronic states in the forbidden band of γ-Al₂O₃, were observed. This study focuses on the effect of the calcination temperature on a γ-Al₂O₃-TiO₂ catalyst (15% *w/w* of TiO₂) and its impact on photocatalytic activity. The catalysts prepared here were characterized by X-ray diffraction, N₂ adsorption–desorption, FTIR-pyridine adsorption, MAS-NMR, HRTEM-FFT, UV-vis, and fluorescence spectroscopy.

**Keywords:** γ-Al₂O₃-TiO₂; acidity; phenol; photodegradation

## 1. Introduction

The extensive use of water reservoirs has provoked serious shortages in many parts of the world [1]. Nowadays, there are several industries that generate large volumes of effluents that are refractory in nature, such as phenols, phenol derivatives, and other toxic compounds [2,3]. Phenolic compounds are classified as persistent organic pollutants (POPs) and are widely found in effluents from industries such as textiles, paper, oil refining, pharmaceuticals, polymers, pesticides, petrochemicals, etc. [4]. The US EPA has listed phenolic compounds as priority pollutants while in most countries, the maximum allowable concentration of phenols in effluent streams is under 1 ppm [5]. The most common treatment applied worldwide to remove aqueous phenols is biological treatment, but high concentrations of phenols can inhibit performance or can even be toxic to the microorganisms employed to remove such contaminants [6]. When using adsorption processes instead, the cost of production increases significantly due to the low adsorption capacity exhibited for these kinds of pollutants (in addition to being limited by the range of the pH of industrial

effluents) [7–9] and low reusability, as the cost of the treatment of used sludge represents from 25 to 65% of the total cost [10].

In the last decades, advanced oxidation processes (AOPs) have become relevant due to the multiple advantages they offer. Among these are the following: with the appropriate catalyst, a series of free radicals including hydroxyl radicals (●OH), ozone ($O_3$), and superoxide radicals ($O_2-●$) [7,10,11] can be generated, which are able to mineralize a wide range of toxic and recalcitrant organic compounds towards $CO_2$ and $H_2O$, avoiding the generation of toxic by-products and reducing the photodegradation time [10]. In addition, low operating costs (since the main source of energy required comes from the sun) and the use of environmentally friendly catalysts make it an advantageous alternative [8,10]. Furthermore, AOPs have proven to be efficient in degrading and mineralizing up to 100% of such molecules [12]. In recent years, some researchers have studied a variety of practical strategies to develop photocatalysts by attempting to mineralize these compounds into water and $CO_2$ [13]. The efficiency of a photocatalyst (defined as the ratio of the percentage of removal of the concentration after time to the initial concentration of the organic contaminant in a solution) depends mainly on its chemical nature. Some of the important parameters are the band gap (between the valence band and the conduction band) and the amount of surface exposed to incident light [14], which in turn depend not only on the macroscopic architecture but also on the specific surface area, structure, and selectivity (key factors for the adsorption process) [15–19]. Nowadays, adsorbent nanomaterials are available to be used as photocatalysts [20,21]. Nanoscale $\gamma$-$Al_2O_3$ can be used in this fashion, but its large band gap energy of about 9 eV [19] makes it difficult for it to behave as a good photocatalyst, so it is necessary to combine it with an adequate solid and use them as mixed oxides [21]. $\gamma$-$Al_2O_3$ offers many advantages, such as a high surface area, great thermal resistance, a good cost-effectiveness ratio, and easy processing for various morphologies. For the purpose of this work, the most significant property is the following: $\gamma$-$Al_2O_3$ possesses many hydroxyl groups distributed all over its surface, making AlO(OH) prone to interact with a wide range of foreign molecules. In this manner, various functional composite materials can be prepared [22,23]. Among the many different materials used as photocatalysts, titanium dioxide ($TiO_2$) is one of the most promising photocatalysts for several applications, such as organic pollutant degradation [23]. Contrary to $\gamma$-$Al_2O_3$, $TiO_2$ has low specific area, does not have good thermal resistance, and exhibits a short time lap for the formation of the electron–hole pair. These disadvantages cause lower photocatalytic activity [6,12–20]. Photocatalysis is one of the most advanced oxidation processes (AOPs), where highly reactive hydroxyl radicals (●OH) are formed and contacted to contaminants in order to degrade them into species such as $CO_2$, $H_2O$, or harmless inorganic anions [19]. Photocatalysis has gained more attention for the decomposition of recalcitrant organic pollutants in the environment [24–27]. A good photocatalyst can be activated by any light higher in energy than its band gap energy. When photocatalysts are irradiated with ultraviolet (UV) light in the presence of $H_2O$ and $O_2$, different reactive oxygen species are generated through reactions of electron ($e^-$)–hole ($h^+$) pairs. $\gamma$-$Al_2O_3$-$TiO_2$ mixed oxides have proved to be excellent photocatalysts [24]. It has been reported that $\gamma$-$Al_2O_3$-$TiO_2$ has effectively increased photocatalytic activity [19–25,28–32]. In this work, a $\gamma$-$Al_2O_3$-$TiO_2$ mixed oxide was synthesized with the peptization of a boehmite method in an effort to improve the photocatalytic performance for the degradation and mineralization of phenols. It is important to highlight that the treatment temperature for a catalyst plays a key role in its activity since it defines its physicochemical properties. The present work focuses on the effect of the calcination temperature of the AT15 catalyst in a range from 400 to 800 °C, which is part of a series of catalysts studied in a previous work [17]. The aim is to find an optimal treatment temperature, as well as to understand the physicochemical properties that it provides to the catalyst.

## 2. Materials and Methods

The γ-Al$_2$O$_3$-TiO$_2$ mixed oxide was prepared through hydrolysis using the boehmite method with titanium alkoxide (modified sol-gel method) [17,26]. The necessary amount of boehmite was placed in a flask, and nitric acid was added until an ideal pH was obtained. Subsequently, isopropanol was added, and it was brought to a temperature of 60 °C, maintaining constant stirring for 24 h. Then, the system was brought to room temperature and the amount of titanium IV isopropoxide necessary to obtain material at 15% the weight of TiO$_2$ was added to the peptized boehmite. The materials were dried and placed in an oven at 120 °C for 12 h. Finally, the materials were calcined under airflow (60 mL min$^{-1}$) at different temperatures (400, 500, 600, 700, and 800 °C) for 6 h [26].

### 2.1. Nitrogen Adsorption

A Quantachrome NOVA 4200e instrument was used to determine the specific surface area from N$_2$ adsorption–desorption isotherms at 77 K. BET and BJH methods were employed to calculate the specific surface area and mean pore diameter, respectively.

### 2.2. X-ray Powder Diffraction

A Bruker D-8 Advance DRX (CuK$_\alpha$ radiation, graphite secondary-beam monochromator, scintillation detector) was utilized to obtain X-ray diffraction patterns between 10 and 80° with a 2θ step of 0.02° (counting time of 9 s). The identification of crystalline phases was performed using the JCPDS database.

The Scherrer equation (L = Kλ/(B(θ)cosθ)) was used to calculate the average crystallite sizes. Interplanar spacing d$_{(hkl)}$ was calculated using Bragg's law: nλ = 2d$_{(hkl)}$sinθ. Due to both anatase and rutile crystallizing in a tetragonal lattice cell, the cell parameters were calculated using $\frac{1}{d_{(hkl)}^2} = \frac{h^2}{a^2} + \frac{h^2}{a^2} + \frac{l^2}{c^2}$ and by choosing reflections at ~37.79 and 48.04° (2θ) for the anatase phase and 27.43 and 62.75° (2θ) for the rutile phase. Since γ-Al$_2$O$_3$ crystallizes in cubic lattices, the cell parameter *a* was obtained from a = 4d$_{(400)}$ using the reflection found at 45.90° (2 θ).

### 2.3. Band Gap Determination

Band gap energies for the series AT-X were calculated using a UV-vis Agilent Cary 100 spectrophotometer equipped with a diffuse reflectance integrated sphere.

### 2.4. FTIR Spectroscopy for the Adsorption of Pyridine

The pyridine adsorption analysis was performed with a Nicolet 170-SX FTIR spectrophotometer. Thin wafers were prepared from the powdered samples and placed in a vacuum-lined Pyrex glass cell provided with CaF$_2$ windows. The samples were evacuated (10$^{-3}$ Torr) at 673 K for 30 min. Then, pyridine was introduced into the system when it reached room temperature. After 30 min, excess pyridine was vacuum-extracted so that the FTIR spectra could be obtained at various temperatures. The acid sites were measured from the integrated absorbance bands using an extinction coefficient, as previously reported in [26].

### 2.5. Fluorescence Technique

The fluorescence detection of ●OH radicals was performed using a 0.5 mM terephthalic acid solution, which was added to 2 mM NaOH and 0.20 g of each catalyst. After stirring for 1 h in the absence of UV light to reach adsorption–desorption equilibrium between the photocatalysts and the terephthalic acid, UV irradiation started (UV mercury lamp Pen-Ray, 254 nm, 4400 mW/cm$^2$). Aliquots of 3 mL were taken every 15 min during 1 h using membrane filters of 0.45 mm. The samples were then analyzed with a Perkin-Elmer LS-50B Luminescence Spectrometer. 2-hydroxyterephthalic acid was formed as the product of the hydroxylation reaction, showing a characteristic fluorescence spectrum (lambda e lambda = 315 nm, lambda em = 425 nm).

*2.6. High-Resolution Transmission Electron Microscopy*

Micrographs were obtained using a JEOL HRTEM 2010F with a field emission source and an acceleration voltage of 200 kV. The powdered samples were dispersed ultrasonically in butanol and then placed on a copper grid and coated with a thin layer of amorphous carbon. In order to measure the crystallographic planes, a digital micrograph program from Gatan Software Team was used.

*2.7. Photocatalytic Evaluation*

The photocatalytic evaluation of the calcined materials was carried out in a glass reactor with a cooling jacket using 200 mL of a solution of phenols with a concentration of 40 ppm and 100 mg of catalyst. A UV Pen-Ray lamp (254 nm and 4400 $\mu W/cm^2$) protected with a quartz tube was immersed in the solution as the source of irradiation. The degradation of phenol was measured by taking aliquots of the solution using a syringe with a nylon membrane in order to remove the suspended solid particles. The evolution of the photodegradation was followed using the phenol adsorption band at 269 nm with a Cary 100 UV-vis spectrophotometer. The mineralization of phenol was measured with TOC determination using Shimadzu LSN equipment.

**3. Results and Discussion**

Figure 1 shows the XRD powder patterns of the catalyst thermally treated at temperatures from 400–800 °C using a methodology called boehmite peptization. It was noted that the diffraction peaks at $2\theta$ = 37.6, 45.8, and 67 were assigned to the (311), (400), and (440) planes corresponding to the $\gamma$-$Al_2O_3$ phase, which were seen in all the samples in accordance with JCPDS No. 50-0741. Moreover, it was observed that the materials treated in the range from 500 to 800 °C exhibited diffraction peaks at $2\theta$ = 25.3, 37, 48.6, and 53.5°, which were assigned to the (101), (004), and (200) planes corresponding to the anatase phase (JCPDS No. 21-1272). Here, it was observed that the calcination temperature played an important role since, as it increased, the nucleation of $TiO_2$ also increased, giving way to the formation of a more defined structure, as reported by Ismail et al. [27,33–35]. For this reason, the crystal size was also affected by the treatment since the crystal size of $\gamma$-$Al_2O_3$ in the 311 plane presented a crystallite size that ranged from 4.88 to 4.79 nm for materials treated from 400 to 700 °C, showing a decrement as the temperature increased. In another case, when the material was treated at 800 °C, the crystallite size increased from 4.79 to 4.83 nm. It should be noted that all the materials exhibited the anatase phase except AT800, which already presented a rutile phase peak. This suggests that both alumina and anatase presented an interaction that allowed them to stabilize the crystalline phase. The crystallite size was observed in a previous work [26]. However, this interaction was no longer possible at 800 °C because the rutile phase of $TiO_2$ appeared, as can be seen in the diffractograms in Figure 1. On the other hand, the crystallite size of the anatase phase in the 101 plane was also affected because the size of the crystal decreased with the effect of the treatment temperature, presenting a crystallite size for plane 101 that varied from 3.93 to 3.96 nm. These values are presented in Table 1.

Figure 2a shows the isotherms for materials synthesized and calcined at temperatures of 400, 500, 600, 700, and 800 °C. Type V isotherms were observed in all the cases. This type of isotherm corresponded to type III due to the weak interactions between adsorbate–adsorbent and the materials present conformed by micro and mesopores. This type of hysteresis was of the H2b type that is associated with materials with blocked pores and with wide pore diameter distributions [36]. The materials calcined from 400 to 600 °C showed the highest values of specific surface area, while materials calcined above 600 °C had a considerable decrease in specific area: 232 $m^2/g$ for the sample calcined at 700 °C and 179 $m^2/g$ for the sample calcined at 800 °C (Table 1). We observed that the specific area decreased as the calcination temperature increased. This is because the materials had a certain thermal resistance. However, once it was exceeded, the walls that made up the structure tended to collapse. On the other hand, as shown in Figure 2b, we observed a

change in pore diameter as the calcination temperature increased. This could be due to aluminum being partially covered and substituted by titanium ions, inducing a lattice expansion due to the smaller $Al^{3+}$ ionic radii [27,29,31,32]. However, it is important to note that the samples calcined at 600 and 700 °C showed smaller pore diameters, especially AT600, unlike the other samples since it was clearly observed that these samples had diameters in the range of 30 to 60 Å, and the other samples had pore diameters in the range of 40 to 120 Å, as can be seen in Figure 2b. The values are reported in Table 1. The effect of this behavior could be due to the displacement of Ti atoms by Al due to the synthesis method, and since the atomic radius of Al is smaller than that of Ti, they were obtained at these temperatures. However, the material calcined at 600 °C presented a greater decrease in pore diameter because aluminum interacted more with Ti. This behavior was assessed in the NMR analysis, and perhaps there was a greater number of displacements of Al atoms by Ti atoms [17]. Regarding pore volume, we observed that, as the treatment temperature increased, this decreased, perhaps because $\gamma$-$Al_2O_3$ pores were obstructed by Ti, and the treatment temperature allowed a greater dispersion on the surface of the alumina.
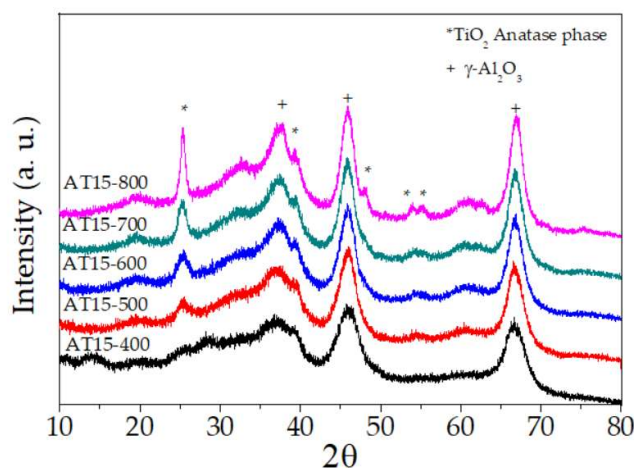


**Figure 1.** Powder X-ray diffraction data of the $\gamma$-$Al_2O_3$-$TiO_2$ catalyst thermally treated in the 400–800 °C range.

**Table 1.** Superficial analysis of the samples.

| Catalysts | Surface Area $m^2/g$ | Total Acidity ($\mu mol/g_{cat}$) | $\gamma$-$Al_2O_3$ * Crystallite Size nm | Anatase + Crystallite Size nm | $D_p$ (Å) | $V_p$ ($cm^3/g$) |
|---|---|---|---|---|---|---|
| AT400 | 308 | 140 | 4.88 | 3.95 | 50–65 | 0.51 |
| AT500 | 266 | 172 | 4.84 | 3.93 | 60 | 0.46 |
| AT600 | 262 | 314 | 4.82 | 3.95 | 45 | 0.41 |
| AT700 | 232 | 270 | 4.79 | 3.96 | 50 | 0.40 |
| AT800 | 179 | 260 | 4.83 | 3.97 | 65 | 0.39 |

* calculated based of the 311 plane of $\gamma$-$Al_2O_3$. + calculated based of the 101 plane of anatase phase of $TiO_2$. $D_p$: pore diameter; $V_p$: pore volume.

Figure 3a shows the UV-vis spectra for the AT series at different temperatures, while a Kubelka–Munk (KM) absorption plot of the same materials is shown in Figure 3b. The KM absorption was obtained from the corresponding reflectance spectra of AT600 with the following relation:

$$R = \frac{(1-R)^2}{2R} \tag{1}$$

where R is the reflectance. Two main signals of absorption at around 320 nm (3.4 eV) and around 400 nm (2.4 eV) were observed. The first one was the result of the charge transfer from $O^{2-}$ to $Ti^{4+}$ corresponding to the excitation of the electrons from the valence band

(O 2p) to the conduction band (Ti 3d), which is characteristic for $TiO_2$ in the anatase phase. This band may also be associated with the morphology of the particles of titanium oxide formed on the surface of the alumina. It has been reported that the shift of the absorption band towards the visible range may be due to the introduction of structural defects into the system, resulting in the formation of intermediate energy states in the band gap of $TiO_2$. Other studies have also reported that this absorption can be associated with the presence of $Ti^{3+}$ ions that, in turn, respond to oxygen vacancies or oxygen-related defects in the range of 2–2.75 eV. Thus, the second band at 400 nm could be assigned to oxygen-related defects caused by a reduction in $TiO_2$ after heat treatment [37–40]. The values are reported in Table 2.
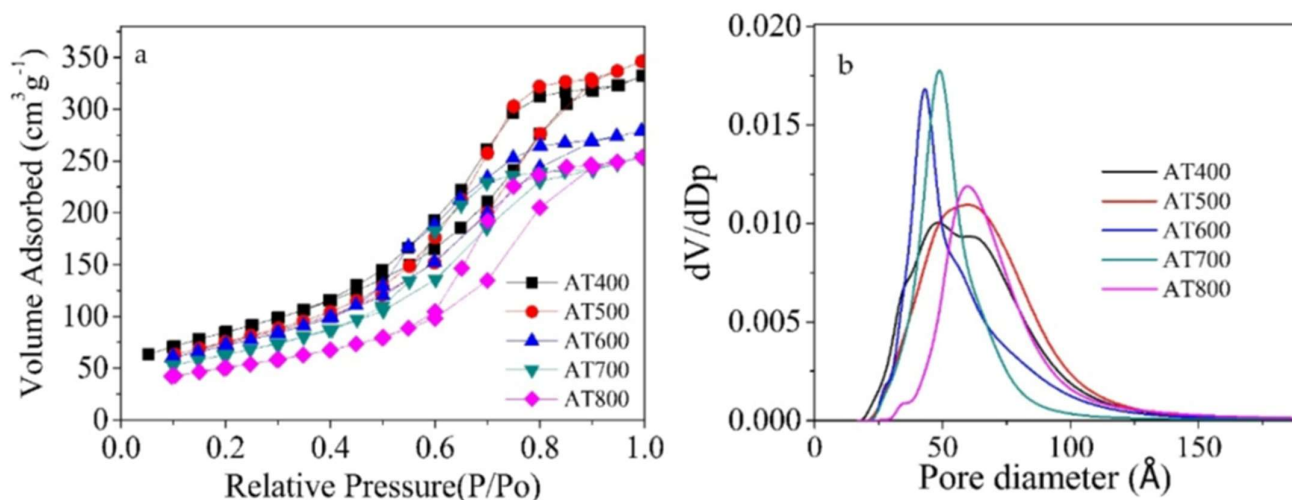


**Figure 2.** (**a**) Nitrogen adsorption−desorption isotherms and (**b**) pore diameter of materials of AT series calcined at different temperatures.
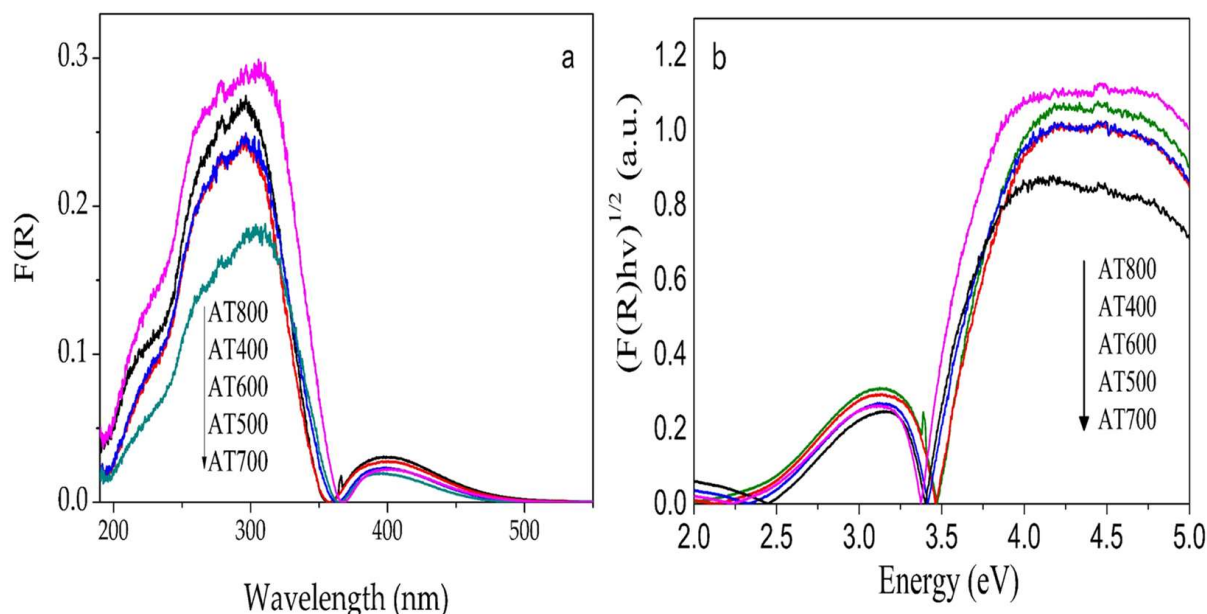


**Figure 3.** UV-vis diffuse reflectance spectra (**a**) and Tauc plot (**b**) for the AT series calcined at different temperatures.

The $^{27}$Al MAS-NMR spectra for the samples treated at different temperatures are shown in Figure 4a. It can be seen that the coordination of the aluminum atom in the AT series was affected by the calcination temperature. It was observed that, for the peak relative to tetracoordinate aluminum (around 70 ppm), it shifted to low field values,

especially for the material calcined at 600 °C (Figure 4b). The changes in the relative abundance of Al(IV) and Al(VI) were also relevant since it has been noticed in previous works that Al(IV) is able to create electronic deficiencies in alumina (as well as increasing acidity), which suggests a synergistic effect between $TiO_2$ and $Al_2O_3$. This behavior is significant since it has been claimed to be responsible for the delay in the recombination of hollow-electron pairs [37,39–41].

**Table 2.** Band gap energy (Eg), half time, and apparent first-order reaction constant for the AT series.

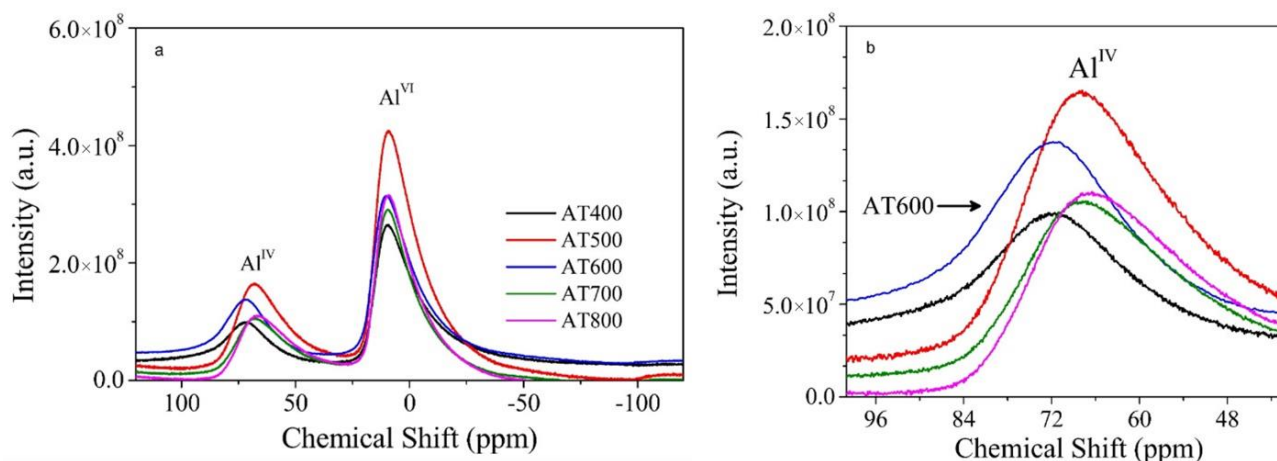| Catalysts | Band Gap Eg (eV) | | $k_{app}$ $\times 10^{-3}$ | $t_{1/2}$ (min) |
|---|---|---|---|---|
| | a | b | | |
| AT400 | 3.3 | 2.30 | 2.1 | 270 |
| AT500 | 3.5 | 2.35 | 2.2 | 255 |
| AT600 | 3.4 | 2.40 | 2.5 | 217 |
| AT700 | 3.4 | 2.50 | 2.1 | 270 |
| AT800 | 3.35 | 2.40 | 1.8 | 325 |



**Figure 4.** (**a**). $^{27}$Al MAS-NMR spectra for the AT calcined at different temperatures, (**b**). attenuation of Al$^{IV}$.

An FTIR spectroscopy analysis of the adsorbed pyridine was performed to determine the acidity of the materials calcined at the given temperatures. Figure 5 shows the spectra that were obtained. Here, two peaks were easily distinguished at 1450 and 1490 cm$^{-1}$. The first, at 1450 cm$^{-1}$, was characteristic of Lewis acidity, and the second, at 1490 cm$^{-1}$, corresponded to the total acidity (no Brønsted acidity, which is located around 1550 cm$^{-1}$). Interestingly, AT600 resulted in a material with an enhanced amount of Lewis acidity (314 μm/g) unlike the others, which exhibited acidities from 140 to 270 μm/g. These values are listed in Table 1. According to the reviewed literature, acidity sites in $TiO_2$ depend on the migration of "bulk" -OHs to the surface since the determination of the Lewis acidity of $TiO_2$ is made by measuring only the hydroxyl groups on the surface. $Ti^{4+}$ ions are potential electron-charge acceptors, i.e., acids, which favor the activity of a material with a greater number of acid sites [33,37,42–48]. For its part, tetracoordinated Al provides strong acid sites, depending on the treatment temperature, since it has been observed that stronger acid sites are obtained as it increases [48,49]. This suggests efficient activity in catalytic photodegradation reactions since the catalytic properties are directly related to the number of acidic (and basic) surface sites.
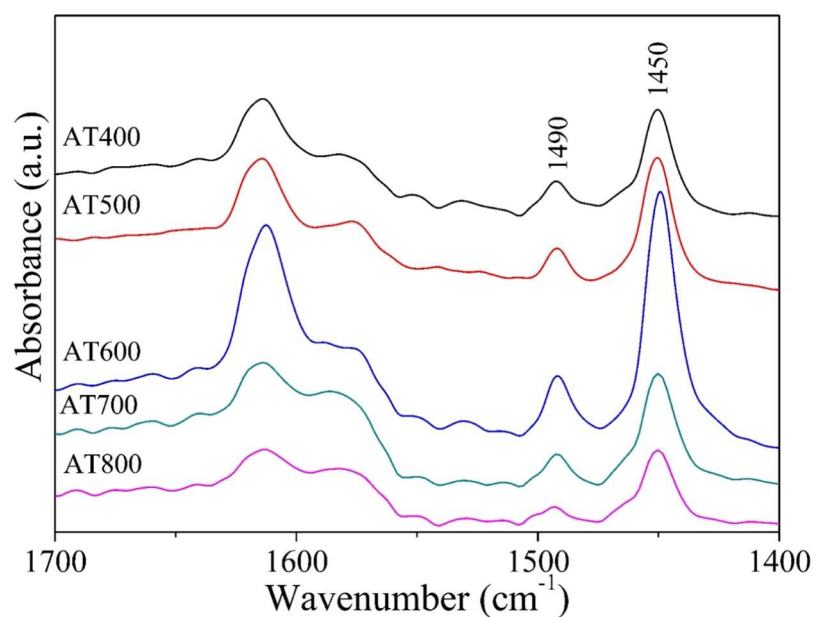
**Figure 5.** DR-FTIR spectra for adsorption of pyridine for the AT series in the spectral region of 1700–1400 cm$^{-1}$.

In Figure 6, HRTEM microscopy is presented for the AT600 catalyst with its respective fast Fourier transform (FFT) patterns for the scanned areas. The assignment of different spacing diffraction patterns for TiO$_2$ in the anatase phase (JCPDS 21-1272 PDF Quality: Star (*)) and γ-Al$_2$O$_3$ (JCPDS 56-0457 Quality PDF) was used. The spacings found in the FFT for the corresponding phase and crystallographic planes with distances of 3.52, 1.66, 2.37, and 2.33 Å, respectively corresponding to the planes (1,0,1) (2,1,1), (0, 0.4), and (1,1,2) for crystalline TiO$_2$ in the anatase phase, can be seen in the FFT (a–d). The distances of 2.28 Å (b,c) and 1.97 Å (c,d) in the FFT corresponded to the crystallographic planes (2,2,2) and (4,0,0) of the γ-Al$_2$O$_3$, crystalline phase [49–51].
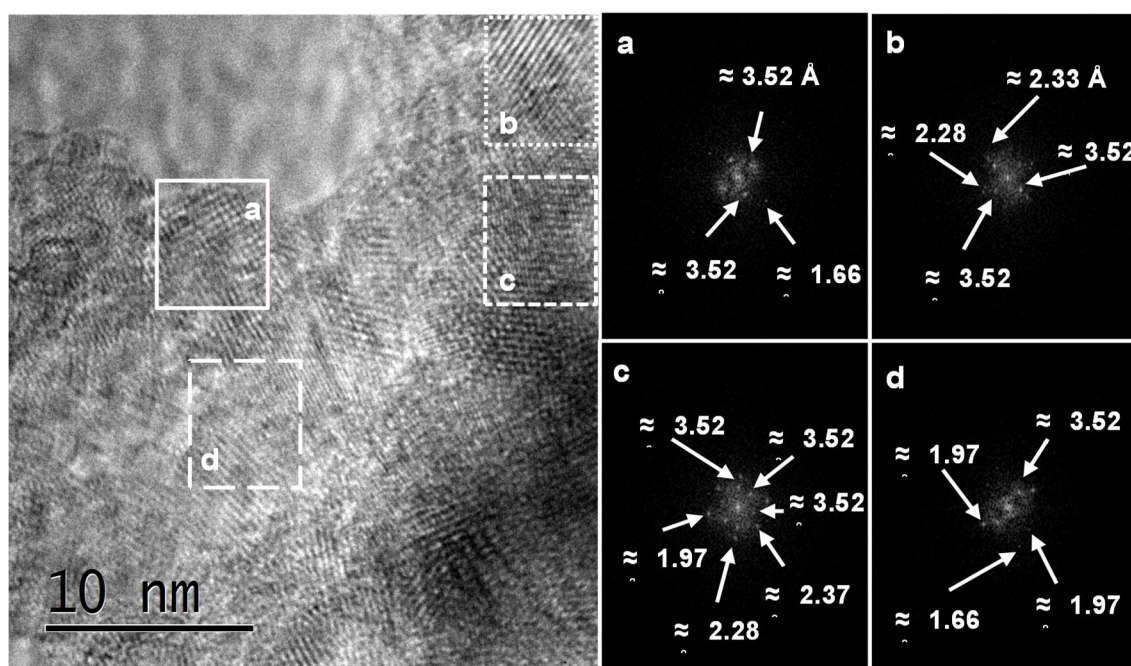


**Figure 6.** High-resolution micrograph (HRTEM) and fast Fourier transform (FFT) of the respective scanned area (**a**–**d**) for the AT600 catalyst calcined at 600 °C.

The absorption of an adequate photon by an electron (e$^-$) of the valence band in a photocatalyst excitates it to the conduction band, creating an electron vacancy or hole (h$^+$), generating electron–hole pairs [15,19,20]. The results presented here indicate that the introduction of alumina acted as a charge transfer catalyst [15,36], so excited electrons from TiO$_2$ could be transferred to alumina, delaying the electron–hole pair recombination. Thus, the electrons generated were rapidly adsorbed on the structural defects of the alumina. Then, the photoinduced holes could oxidize $^-$OH ions or H$_2$O adsorbed on the surface, producing highly oxidizing ●OH species. The rate of this process is a competition between the oxidation of surface water by the holes and the limiting electron–hole recombination time [52]. The ●OH radicals are assumed as the main species responsible for the photocatalytic oxidation of chemicals [37,52,53]. In order to detect ●OH radicals formed on the AT600 material, it was irradiated under UV light with a fluorescence technique using terephthalic acid. In Figure 7, it can be seen that the emission spectra of the terephthalic acid solution were obtained every 15 min. The spectra obtained showed a gradual increase in fluorescence at around 425 nm for both the AT600 material and the reaction system without the catalyst. The intensity of the peak was related to the amount of ●OH radicals formed [46]. The same procedure was also carried out without the catalyst to corroborate the generation of ●OH radicals in the reaction by the AT600 catalyst.
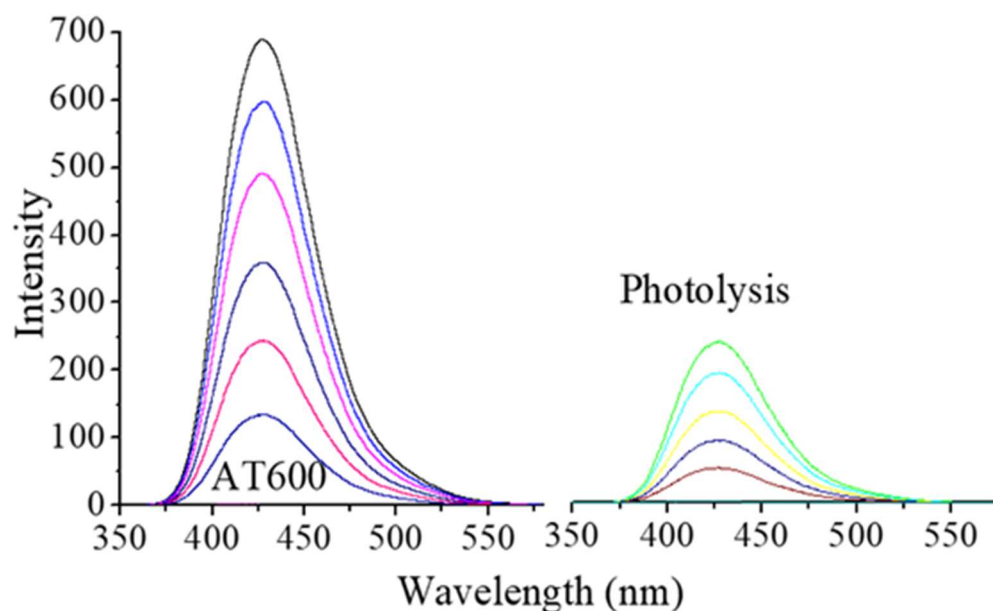


**Figure 7.** Fluorescence spectra of terephthalic acid during irradiation of the AT600 photocatalyst under UV light for 1.5 h and photolysis.

## 4. Photocatalytic Evaluation

The photocatalytic activity of AT series was evaluated under the mineralization of 40 ppm phenol. Figure 8a shows the results after one hour in darkness to allow an adsorption–desorption equilibrium of phenol molecules on the catalyst surface. Photolysis of the phenol molecules was carried out during 360 min in the same way that the catalytic photodegradation reactions transpired with the catalysts. During this reaction, it was possible to observe that there was no mineralization of phenol due to the effect of the UV lamp. Furthermore, the molecules were not adsorbed during the first 60 min of the reaction. In addition to this reaction, the photodegradation reactions were observed with the AT catalysts calcined at different temperatures (400 to 800 °C). We observed that the catalyst thermally treated at 600 °C showed the highest activity (Figure 8a), and this behavior was corroborated with the TOC analysis. It was clearly observed that AT600 catalyst showed the greatest activity since it presented the highest degradation of the molecule, as seen in Figure 8b.
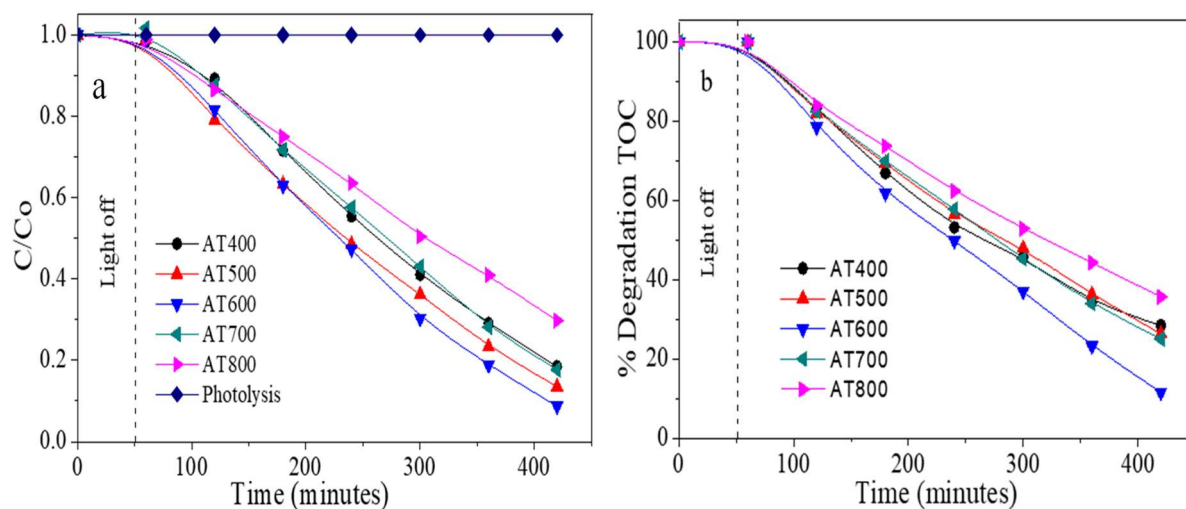
**Figure 8.** (**a**) C/Co vs. time plots for phenol photodegradation after irradiation with UV-vis light, and (**b**) percentage of degradation on TOC.

When following the photodegradation of phenol with a UV-vis spectrophotometer, the following behavior was observed: the most active photocatalyst was the one that was treated at 600 °C, followed by the catalysts treated at 500 > 700 > 400 > 800 °C. This was corroborated by the TOC analysis, where the activity of AT600 resulted as the most active. However, the activity levels of the other materials varied in the following order: AT600 > AT700 > AT500 > AT400 > AT800. This demonstrated that the treatment temperature during the oxidation of material is crucial for the performance of the photocatalyst since it defines its physicochemical properties. Furthermore, the apparent kinetics ($K_{app}$) for the photodegradation of phenol were obtained by the Langmuir–Hinshelwood formalism, which applies for pseudo-first-order in the photodegradation of phenol. As shown in the graph of ln C/Co versus time (Figure 9) [54,55], the $k_{app}$ values and half-life time for the reactions were also obtained, as reported in Table 2.
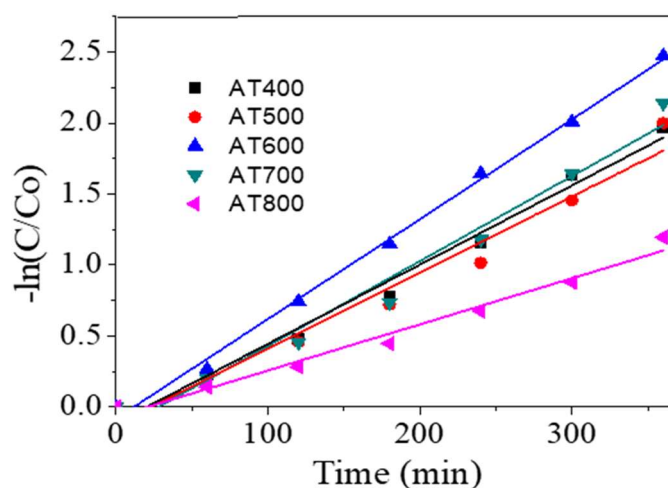


**Figure 9.** Pseudo-first-order kinetics for the photodegradation of phenol for the AT series.

In order to better understand this mechanism of catalytic degradation, a band diagram for the $\gamma$-$Al_2O_3TiO_2$ catalysts is presented in Figure 10. As can be seen in Figure 7, the mechanism of this catalysts was *OH radicals, which were formed as soon as the catalyst entered into contact with the reaction system and the energy of the lamp [17]. This was possible since the synthesis methodology allowed the formation of a staggered-gap-type heterojunction between $TiO_2$ and $\gamma$-$Al_2O_3$, facilitating electronic transfers from $TiO_2$ to

alumina and delaying $h^+$–$e^-$ recombination time [56,57]. This does not rule out another type of reaction, but this can be verified in future work.
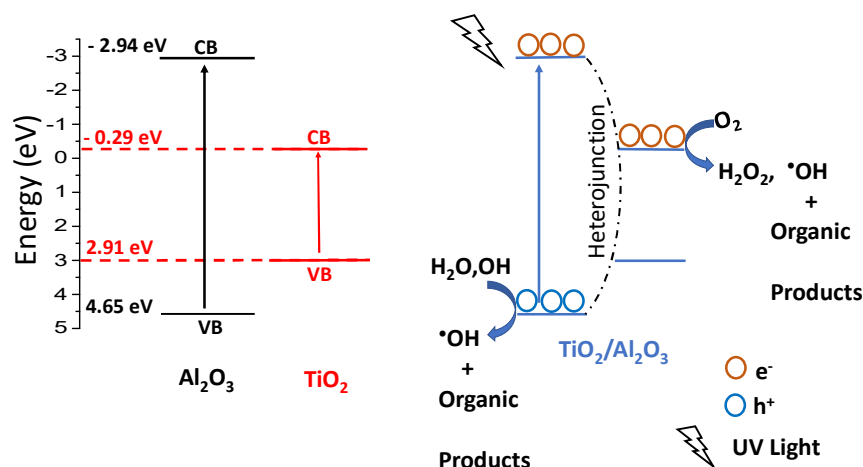


**Figure 10.** Band diagram for $\gamma$-$Al_2O_3$ with $TiO_2$ catalysts.

In Figure 11a a study of catalyst reuse is shown. It was observed that, after three cycles of 360 min each, the catalyst only lost 13% of its photoactivity, which confirmed that, when $\gamma$-$Al_2O_3$ interacted with $TiO_2$, a synergistic effect was generated that allowed the catalyst to stabilize, obtaining a material with superior physicochemical stability. This was corroborated by the TOC analysis Figure 11b.
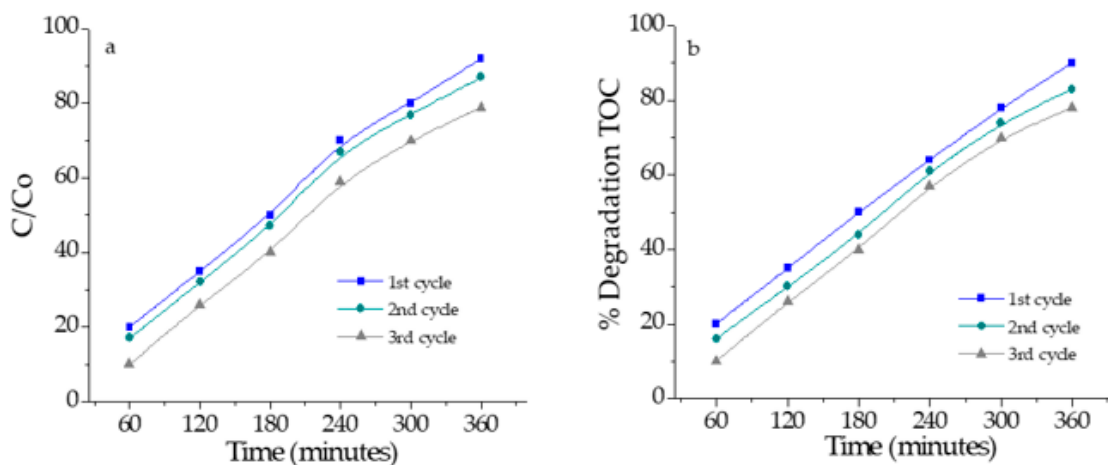


**Figure 11. (a)** Catalyst reuse study with UV-Vis spectroscopy. **(b)**TOC analysis.

## 5. Operating Cost

Along with the investigation of the mass and energy balances, a study was carried out on the cost benefit of the phase contemplated. Qualified pretreatment is crucial before applying it in a pilot plant. Discrete costs, such as the cost of the removal of sludge biosolids, operating costs (including the costs of chemicals and energy), and the cost of the removal of reduced sludge biosolids after treatment, were considered for the evaluation of the feasibility of the adopted pretreatment method. In view of this, the energy cost (biomethane) and the cost of the depletion of biosolids were conceived as cost-effective (gain), while the chemical cost and the cost of surplus biosolids after treatment were recognized as a loss of benefits.

The cost distribution of different AOPs in different mineralization targets in Europe and the USA range from 0.031 to 0.040 USD/m$^3$. Following an analysis of the entire process, the main expense was chemicals, followed by electricity for fluid recirculation, regardless of the

mineralization performance. Overall, for a target of 99% mineralization, chemicals accounted for 90% of the overall cost, while the contribution of electricity accounted for 10%.

Despite this, it is important to point out that the generated sludge volume would represent around 10% of the wastewater treated in photocatalytic processes, generating non-negligible management costs. However, it could be said that the main advantage of heterogeneous processes is the impact of a reduction in chemical costs by avoiding adjusting the pH to 3.

Further pilot plant and industrial-scale studies on real wastewater matrices are required to validate the suitability of the photocatalytic criterion and to compare them with traditional plants.

## 6. Technical Feasibility and Applicability

Most $\gamma$-$Al_2O_3$-based catalysts exhibit excellent reuse, stability, and biocompatibility for the degradation of organic pollutants. Despite the progress made so far, there are still many challenges for alumina-based catalysts in the degradation of organic pollutants in water. Some points are listed below:

- Photocatalytic rates and the stability of $\gamma$-$Al_2O_3$-based catalysts can be further improved. In spite of the high degradation rates achieved so far, the percentage of mineralization can be increased. Furthermore, the stability levels of some catalysts based on $\gamma$-$Al_2O_3$ are still unsatisfactory due to the loss of active sites and the leaching of metal dopants. Therefore, it is important to optimize catalyst synthesis methods and to develop new types of catalysts based on $\gamma$-$Al_2O_3$ that are more active and stable.
- The mechanism involved in the degradation of organic pollutants and the toxicity of the reaction intermediates should be thoroughly investigated. A theoretical study based on DFT could reveal the most preferential sites to be attacked (and the possible reaction intermediates) for target contaminants. In addition, it is necessary to evaluate the ecotoxicity and human toxicity of such intermediates since they can result in even more toxicity than the original moieties.
- The performances of photocatalysts must be evaluated using actual wastewater. There are important differences between simulated and actual wastewater that make results obtained for simulated wastewater less accurate.
- Experiments should be conducted on a major scale. Until now, most research on $\gamma$-$Al_2O_3$-based catalysts for the degradation of organic pollutants has been performed at lab-scale reactors. More attention should be paid to the reactor design, as well as to scaling Figure 12.
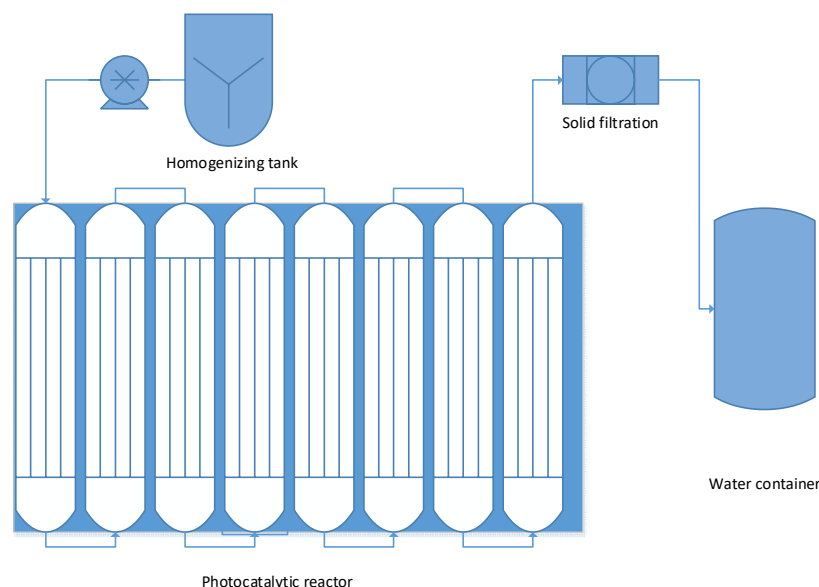


**Figure 12.** Proposed design for a pilot plant.

## 7. Conclusions

The methodology of synthesis presented here allowed the formation of staggered-gap heterojunctions, making it easy to transfer electrons from $TiO_2$ to alumina and delaying $h^+$–$e^-$ recombination time. This synthesis method was fast, efficient, and simple, and due to this, we could call it a green synthesis.

The increase in specific area obtained using $\gamma$-$Al_2O_3$ favored the activity of the $TiO_2$ photocatalyst since the adsorption of the contaminant molecules on the surface was enhanced, leading to superior photodegradation.

The catalysts treated below 700 °C showed only the characteristic peaks for the gamma phase of alumina and the anatase phase for $TiO_2$. However, the material treated at 800 °C also presented a low-intensity peak of the rutile phase in its 110 plane, which indicated that the $\gamma$-$Al_2O_3$ stabilized the anatase phase of $TiO_2$ below 800 °C. On the other hand, a decrease in the specific area values was also observed when the temperature increased, as well as changes in pore diameter distribution, showing pore diameters of 30–60 Å for the catalyst treated at 600 °C and pore diameters ranging from 30 to 120 Å for the rest of the materials. In the account of band gap values, two signals were observed: the first was the typical signal of the interaction of Ti with oxygen, and the second indicated that $Ti^{3+}$ ions were present that were related to oxygen deficiencies. On the other hand, NMR data showed a low field shift for tetracoordinate aluminum, especially for the AT600 catalyst. Al(IV) is related to a deficiency of electrons in the alumina, so it acted as an electron trap in the reaction, agreeing with the results obtained when determining acidity with pyridine sorption since the AT600 material had the largest number of acid sites (314 mmol py/$g_{cat}$), followed by the AT700 catalyst (270 mmol py/$g_{cat}$). This parameter was important since acidity is related to oxygen vacancies. Regarding the photocatalytic activity, the AT600 catalyst showed the highest activity since it degraded about 95% of the phenol in 217 min compared to the other catalysts that degraded only about 70% in a range from 255 to 325 min. The same tendency was corroborated with the total organic carbon analysis. It was concluded that treatment temperature largely defined the physicochemical characteristics of the material and, therefore, its activity. Thus, even though all the catalysts started from the same material, differences were observed in the characterizations carried out, as seen in the catalyst treated at 600 °C, which presented the greatest differences in terms of its physicochemical properties and activity.

**Author Contributions:** C.M.-G., I.R.-V., R.Z., G.d.Á., F.T., B.R.-C., E.V.-R. and A.P.-L. contributed to the writing, review, and editing, and all agreed to the published version of the manuscript. All authors have read and agreed to the published version of the manuscript.

**Institutional Review Board Statement:** Not applicable.

**Informed Consent Statement:** Not applicable.

**Data Availability Statement:** Not applicable.

**Conflicts of Interest:** The authors declare no conflict of interest.

## References

1. Hu, Y.; Li, D.; Sun, F.; Weng, Y.; You, S.; Shou, Y. Temperature-induced phase changes in bismuth oxides and efficient photodegradation of phenol and p-chlorophenol. *J. Hazard. Mater.* **2016**, *301*, 362–370. [CrossRef] [PubMed]
2. Eriksson, E.; Baun, A.; Mikkelsen, P.; Ledin, A. Risk assessment of xenobiotics in stormwater discharged to Harrestrup Å, Denmark. *Desalination* **2007**, *2151*, 187–197. [CrossRef]
3. Ahmed, S.; Rasul, M.G.; Martens, W.N.; Brown, R.; Hashib, M.A. Advances in heterogeneous photocatalytic degradation of phenols and dyes in wastewater: A review. *Water Air Soil Pollut.* **2011**, *215*, 3–29. [CrossRef]

4. Mantilla, A.; Tzompantzi, F.; Fernández, J.L.; Góngora, J.D.; Gómez, R. Photodegradation of phenol in aqueous medium by using Zn/Al+Fe mixed oxides obtained from layered double hydroxides materials. *Catal. Today* **2010**, *150*, 353–357. [CrossRef]

5. Mahamuni, N.; Pandit, A.B. Effect of additives on ultrasonic degradation of phenol. *Ultrason. Sonochem.* **2006**, *13*, 165–174. [CrossRef]

6. Karunakaran, C.; Dhanalakshmi, R. Semiconductor-catalyzed degradation of phenols with sunlight. *Sol. Energy Mater. Sol. Cells* **2008**, *92*, 1315–1321. [CrossRef]

7. Wang, J.; Zhuan, R. Degradation of antibiotics by advanced oxidation processes: An overview. *Sci. Total Environ.* **2020**, *701*, 651–669. [CrossRef]

8. Dewil, R.; Mantzavinos, D.; Poulios, I.; Rodrigo, M.A. New perspectives for Advanced Oxidation Processes. *J. Environ. Manag.* **2017**, *195*, 93–99. [CrossRef]

9. Ike, I.A.; Linden, K.G.; Orbell, J.D.; Duke, M. Critical review of the science and sustainability of persulphate advanced oxidation processes. *Chem. Eng. J.* **2018**, *338*, 651–669. [CrossRef]

10. Ahmed, L.M. Bulk and nanocatalysts applications in Advanced Oxidation Processes. In *Oxidoreductase*; BoD–Books on Demand: Norderstedt, Germany, 2021; Volume 7, pp. 107–111. [CrossRef]

11. Miklos, D.B.; Remy, C.; Jekel, M.; Linden, K.G.; Drewes, J.E.; Hübner, U. Evaluation of advanced oxidation processes for water and wastewater treatment e A critical review. *Water Res.* **2018**, *139*, 118–131. [CrossRef] [PubMed]

12. Vazquez, I.R.; del Angel, G.; Bertin, V. Synthesis and characterization of Sn doped $TiO_2$ photocatalysts: Effect of Sn concentration on the textural properties and on the photocatalytic degradation of 2,4-dichlorophenoxyacetic acid. *J. Alloys Compd.* **2015**, *643*, S144–S149. [CrossRef]

13. Thompson, T.L., Jr.; Yates, J.T. Surface Science Studies of the Photoactivation of $TiO_2$, New Photochemical Processes. *Chem. Rev.* **2006**, *106*, 4428–4453. [CrossRef] [PubMed]

14. Xi-yao, Y.; Kai, Z.; Luo, X.; He, J. Inlfuence of $TiO_2$ on surface properties of $Al_2O_3$. *React. Kinet. Catal. Lett.* **1992**, *46*, 179–186. [CrossRef]

15. González, V.; Zanella, R.; del Angel, G.; Gómez, R. MTBE visible-light photocatalytic decomposition over $Au/TiO_2$ and $Au/TiO_2$-$Al_2O_3$ sol-gel prepared catalysts. *J. Mol. Catal. Chem.* **2008**, *281*, 93–98. [CrossRef]

16. Yang, C.; Wang, Y.; Shih, M.; Chang, Y.; Hon, C. Photocatalytic performance of alumina-incorporated titania composite nanoparticles: Surface area and crystallinity. *Appl. Catal. A* **2009**, *364*, 182–190. [CrossRef]

17. Gomez, C.M.; del Angel, G.; Ramos-Ramirez, E.; Rangel-Vazquez, I.; Gonzalez, F.; Arrieta, A.; Vazquez-Zavala, A.; Bonilla-Sanchez, A.; Cantu, M.S. Alumina coating with $TiO_2$ and its effect on catalytic photodegradation of phenol and p-cresol. *J. Chem. Technol. Biotechnol.* **2016**, *91*, 2211–2220. [CrossRef]

18. Mechiakh, R.; Meriche, F.; Kremer, R. $TiO_2$ thin films prepared by sol–gel method for waveguiding applications: Correlation between the structural and optical properties. *Opt. Mater.* **2007**, *30*, 645–651. [CrossRef]

19. Svagelj, Z.; Mandic, V.; Curkovic, L.; Biosic, M.; Zmak, I.; Gaborardi, M. Titania-Coated Alumina Foam Photocatalyst for Memantine Degradation Derived by Replica Method and Sol-Gel Reaction. *Materials* **2020**, *13*, 227. [CrossRef]

20. Cizmic, M.; Ljubas, D.; Rozman, M.; Asperger, D.; Curkovic, L.; Babic, S. Photocatalytic degradation of azithromycin by nanostructured $TiO_2$ film: Kinetics, degradation products, and toxicity. *Materials* **2019**, *12*, 873. [CrossRef]

21. Cano-Casanova, L.; Amorós-Pérez, A.; Lillo-Ródenas, M.A. Román-Martínez, Effect of the Preparation Method (Sol-Gel or Hydrothermal) and Conditions on the $TiO_2$ Properties and Activity for Propene Oxidation. *Materials* **2018**, *11*, 2227. [CrossRef]

22. Lee, S.Y.; Matsubara, T.; Numata, D.; Serizawa, A. Facile Synthesis of Potassium-Doped Titanium Oxide Nanostructure ($KTiO_xs$)/AlO(OH) Composites for Enhanced Photocatalytic. *Catalysts* **2021**, *11*, 548. [CrossRef]

23. Xu, X.; Zu, X.; Ao, D.; Yu, J.; Xiang, X.; Xie, W.; Tang, Y.; Li, S.; Fu, Y. NH3-Sensing Mechanism Using Surface Acoustic Wave Sensor with AlO(OH) Film. *Nanomaterials* **2019**, *9*, 1732. [CrossRef] [PubMed]

24. Lee, J.-W.; Jang, Y.-I.; Park, W.-S.; Kim, S.-W.; Lee, B.-J. Photocatalytic and Pozzolanic Properties of Nano-$SiO_2$/$Al_2O_3$-$TiO_2$ Powder for Functional Mortar. *Materials* **2019**, *12*, 1037. [CrossRef]

25. Roongraung, K.; Chuangchote, S.; Laosiripojana, N. Enhancement of Photocatalytic Oxidation of Glucose to Value-Added Chemicals on $TiO_2$ Photocatalysts by A Zeolite (Type Y) Support and Metal Loading. *Catalysts* **2020**, *10*, 423. [CrossRef]

26. Park, Y.; Kim, S.; Kim, J.; Khan, S.; Han, C. UV/$TiO_2$ Photocatalysis as an Efficient Livestock Wastewater Quaternary Treatment for Antibiotics Removal. *Water* **2022**, *14*, 958. [CrossRef]

27. Marizcal-Barba, A.; Sanchez-Burgos, J.A.; Zamora-Gasga, V.; Perez Larios, A. Study of the Response Surface in the Photocatalytic Degradation of Acetaminophen Using $TiO_2$. *Photochem* **2022**, *2*, 225–236. [CrossRef]

28. Ismail, A.A.; Abdelfattah, I.; Atitar, M.F.; Robben, L.; Bouzid, H.; Al-Sayari, S.A.; Bahnemann, D.W. Photocatalytic degradation of imazapyr using mesoporous $Al_2O_3$–$TiO_2$ nanocomposites. *Sep. Purif. Technol.* **2015**, *145*, 147–153. [CrossRef]

29. Zhang, C.; Chen, H.; Ma, M.; Yang, Z. Facile synthesis of magnetically recoverable $Fe_3O_4$/$Al_2O_3$/molecularly imprinted $TiO_2$ nanocomposites and its molecular recognitive photocatalytic degradation of target contaminant. *J. Mol. Catal. A Chem.* **2015**, *402*, 10–16. [CrossRef]

30. 30. Rodríguez-Barajas, N.; Becerra-Solano, L.; Gutiérrez-Mercado, Y.K.; Macías-Carballo, M.; Gómez, C.M.; Pérez-Larios, A. Study of the Interaction of Ti–Zn as a Mixed Oxide at Different pH Values Synthesized by the Sol–Gel Method and Its Antibacterial Properties. *Nanomaterials* **2022**, *12*, 1948. [CrossRef]

31. Magnone, E.; Kim, M.K.; Lee, H.J.; Park, J.H. Testing and substantial improvement of TiO$_2$/UV photocatalysts in the degradation of Methylene Blue. *Ceram. Int.* **2019**, *45*, 3359–3367. [CrossRef]

32. Vargova, M.; Plesch, G.; Vogt, U.F.; Zahoran, M.; Gorbar, M.; Jesenak, K. TiO$_2$ thick films supported on reticulated macroporous Al$_2$O$_3$ foams and their photoactivity in phenol mineralization. *Appl. Surf. Sci.* **2011**, *257*, 4678–4684. [CrossRef]

33. Shtyka, O.; Ciesielski, R.; Kedziora, A.; Maniukiewicz, W.; Dubkov, S.; Gromov, D.; Maniecki, T. Photocatalytic reduction of CO$_2$ Over Me (Pt, Pd, Ni, Cu)/TiO$_2$ Catalysts. *Top. Catal.* **2020**, *63*, 113–120. [CrossRef]

34. Wang, X.; Cui, J.; Zhang, N.; Song, J.; Fan, X.; Zhao, Z.; Kong, L.; Xiao, X.; Xie, Z. Propane Dehydrogenation over PtSn/Al$_2$O$_3$ Catalysts: Influence of Urea to Al(NO$_3$)$_3$_9H$_2$O Ratio. *Catalysts* **2022**, *12*, 157. [CrossRef]

35. Murillo-Acevedo, Y.; Giraldo, L.; Moreno-Pirajan, J.C. Nanoparticles size distribution and phenol photodegradation with TiO$_2$/C support obtained by phosphoric acid activation of palm kernel shell. *Microporous Mesoporous Mater.* **2020**, *304*, 109325. [CrossRef]

36. Thommes, M.; Kaneko, K.; Neimark, A.V.; Olivier, J.P.; Rodriguez-Reinoso, F.; Rouquerol, J.; Sing, K.S. Physisorption of gases, with special reference to the evaluation of surface area and pore size distribution (IUPAC Technical Report). *J. Pure Appl. Chem.* **2015**, *87*, 1051–1069. [CrossRef]

37. Gómez, C.M.; del Angel, G.; Tzompantzi, F.; Gómez, R.; Torres-Martínez, L. Photocatalytic degradation of p-cresol on Pt/γAl$_2$O$_3$-TiO$_2$ mixed oxides: Effect of oxidizing and reducing pre-treatments. *J. Photochem. Photobiol. A Chem.* **2012**, *236*, 21–25. [CrossRef]

38. Wang, H.-L.; Qi, H.-P.; Wei, X.-N.; Liu, X.-Y.; Jiang, W.-F. Photocatalytic activity of TiO$_2$ supported SiO$_2$-Al$_2$O$_3$ aerogels prepared from industrial fly ash. *Chin. J. Catal.* **2016**, *37*, 2025–2033. [CrossRef]

39. Escobar, J.; de los Reyes, J.A.; Viveros, T. Sol–gel Al$_2$O$_3$ structure modification by Ti and Zr addition. A NMR study. *Stud. Surf. Sci. Catal.* **2000**, *143*, 547–554.

40. Kwak, J.H.; Hu, J.Z.; Kim, D.H.; Szanyi, J.; Peden, C.H.F. Penta-coordinated Al$^{3+}$ ions as preferential nucleation sites for BaO on γ-Al$_2$O$_3$: An ultra-high-magnetic field $^{27}$Al MAS NMR study. *J. Catal.* **2007**, *251*, 189–194. [CrossRef]

41. Li, L.D.; Xu, C.Z.; Zheng, M.Q.; Chen, X.H. Effect of B$_2$O$_3$ modified Ag/TiO$_2$-Al$_2$O$_3$ adsorbents on the adsorption desulfurization of diesel. *J. Fuel Chem. Technol.* **2015**, *43*, 990–997. [CrossRef]

42. Etacheri, V.; di Valentin, C.; Schneider, J.; Bahnemann, D.; Pillai, S.C. Visible-light activation of TiO$_2$ photocatalysts: Advances in theory and experiments. *J. Photochem. Photobiol. C Photochem. Rev.* **2015**, *25*, 1–29. [CrossRef]

43. Kuznetsov, V.N.; Serpone, N. Visible Light Absorption by Various Titanium Dioxide Specimen. *J. Phys. Chem. B* **2006**, *110*, 50. [CrossRef] [PubMed]

44. Pham, H.H.; Wang, L.-W. Oxygen vacancy and hole conduction in amorphous TiO$_2$. *Phys. Chem. Chem. Phys.* **2015**, *17*, 541–550. [CrossRef] [PubMed]

45. Kuznetsov, V.N.; Serpone, N. On the Origin of the Spectral Bands in the Visible Absorption Spectra of Visible-Light-Active TiO$_2$ Specimens Analysis and Assignments. *J. Phys. Chem. C* **2009**, *113*, 15110–15123. [CrossRef]

46. Liu, X.; Truitt, R.E. DRFT-IR Studies of the Surface of γ-Alumina. *J. Am. Chem. Soc.* **1997**, *119*, 9856–9860. [CrossRef]

47. Yang, X.; Song, Y.; Cao, T.; Wang, L.; Song, H.; Lin, W. The double tuning effect of TiO$_2$ on Pt catalyzed dehydrogenation of methylcyclohexane. *Mol. Catal.* **2020**, *492*, 110971. [CrossRef]

48. Liu, X. DRIFTS Study of Surface of α-Alumina and Its Dehydroxylation. *J. Phys. Chem. C* **2008**, *112*, 5066–5073. [CrossRef]

49. Ismail, A.A.; Bahnemann, D.W.; Robben, L.; Yarovyi, V.; Wark, M. Palladium Doped Porous Titania Photocatalysts: Impact of Mesoporous Order and Crystallinity. *Chem. Mater.* **2010**, *22*, 108–116. [CrossRef]

50. Nair, S.B.; John, K.A.; Joseph, J.A.; Babu, S.; Shinoj, V.K.; Remillard, S.K.; Shaji, S.; Philip, R.R. Influence of pn junction mechanism and alumina overlayer on the photocatalytic performance of TiO$_2$ nanotubes. *Nanotechnology* **2020**, *31*, 275403. [CrossRef]

51. Chowdhury, I.H.; Roy, M.; Kundu, S.; Naskar, M.K. TiO$_2$ hollow microspheres impregnated with biogenic gold nanoparticles for the efficient visible light-induced photodegradation of phenol. *J. Phys. Chem. Solids* **2019**, *129*, 329–339. [CrossRef]

52. Ishibashi, K.I.; Fujishima, A.; Watanabe, T.; Hashimoto, K. Quantum yields of active oxidative species formed on TiO$_2$ photocatalyst. *J. Photochem. Photobiol. A* **2000**, *134*, 139–142. [CrossRef]

53. Ishibashi, K.I.; Fujishima, A.; Watanabe, T.; Hashimoto, K. Detection of active oxidative species in TiO$_2$ photocatalysis using the fluorescence technique. *Electrochem. Commun.* **2000**, *2*, 207–210. [CrossRef]

54. Castro, L.V.; Ortiz-Islas, E.; Manríquez, M.E.; Albiter, E.; Cabrera-Sierra, R.; Alvarado-Zavala, B. Photocatalytic Degradation of Mixed Dyes in Aqueous Phase by MgAlTi and ZnAlTi Mixed Oxides. *Top. Catal.* **2020**, *64*, 97–111. [CrossRef]

55. Tzompantzi, F.; Castillo-Rodríguez, J.C.; Tzompantzi-Flores, C.; Pérez-Hernández, R.; Gómez, R.; Santolalla-Vargas, C.E.; Che-Galicia, G.; Ramos-Ramírez, E. Addition of SnO$_2$ over an oxygen deficient zirconium oxide (ZrxOy) and its catalytic evaluation for the photodegradation of phenol in water. *Catal. Today* **2022**, *394–396*, 376–389. [CrossRef]

56. Samuel, O.; Othman, M.H.D.; Kamaludin, R.; Sinsamphanh, O.; Abdullah, H.; Puteh, M.H.; Kurniawan, T.A. WO$_3$–based photocatalysts: A review on synthesis, performance enhancement and photocatalytic memory for environmental applications. *Ceram. Int.* **2022**, *48*, 5845–5875. [CrossRef]

57. Mengting, Z.; Kurniawan, T.A.; Duan, L.; Song, Y.; Hermanowicz, S.W.; Othman, M.H.D. Advances in BIOX-based ternary photocatalysis for water technology and energy storage applications: Research trends, challenges, solutions and ways forward. *Rev. Environ. Sci. Bio/Technol.* **2022**, *21*, 331–370. [CrossRef]